Initial coalescence between a drop and a liquid pool: A lattice Boltzmann investigation validated by experiments

E. Collignon, Q. Zhang, Xavier Frank, Huai Li

Initial coalescence between a drop and a liquid pool: a Lattice Boltzmann investigation validated by experiments

E. Collignon,[1] Q. D. Zhang (张沁丹),[1,2] X. Frank,[3, a)] and Huai Z. Li (李怀志)[1, b)]
[1)] *University of Lorraine, CNRS, LRGP, F-54000 Nancy, France*
[2)] *Institute for Systems Rheology, School of Mechanical and Electrical Engineering, Guangzhou University, Guangzhou 510006, China*
[3)] *IATE, Univ. Montpellier, INRAE, Institut Agro, Montpellier, France*

(Dated: 12 November 2024)

We present a numerical investigation of the coalescence of a drop with a pool of the same liquid. The simulations were carried out with both viscous Newtonian and viscoelastic fluids, based on an axisymmetric high density ratio lattice Boltzmann method with a diffuse interface coupled with the Oldroyd-B Model. Particular attention was paid to the widening dynamics of the liquid bridge between the drop and the pool, and to the velocity fields within both the drop and liquid bulk. The results were compared with experimental data obtained using a high-speed camera and a micro-Particle Image Velocimetry (μ-PIV) and displayed satisfactory agreement. In particular, the simulated temporary evolution of the rescaled coalescing width of the liquid bridge in function of the normalized time compares favorably with the experimental results for both the inertially limited viscous and the inertial regimes for short and long time.

I. INTRODUCTION

Drop coalescence is of both academic and industrial interest and plays a major role in numerous applications including emulsions, foams, oil recovery, mass transfer and reaction between liquids as well as falling raindrops in a pool[1]. From the physical point of view, a drop may bounce, coalesce or splash at the liquid interface according to its initial approaching velocity[2,3] when impinging with a bath of the same liquid. The coalescence of a drop into a pool of liquid can be either instantaneous or delayed[4], complete or partial[5] and affected by various factors including the fluid density[6], surface tension gradient[7], thermal effect[4], ambient pressure[8] or local Marangoni flow[9].

In recent years, experimental investigation on the very initial drop coalescence have been performed, usually be means of visualization with a high-speed camera from side view or both side and bottom view[10–13]. Whatever the coalescence configuration between two drops, or between a drop and a planar liquid surface of the same nature, three regimes were identified through the relationship between dimensionless coalescence width and normalized time: linear in the inertially limited viscous (ILV) regime; logarithmic correction in the transient viscous regime; and finally square root in the inertial regime. It is worth noting that the visualization, based on high-speed camera with typically minimum interval about $0.01ms$, is still far from sufficient to study the dynamics of very initial contact within typical length below 100 μm. Some experiments have been attempted using AC[14] or DC[15] electrical circuits with electrolyte drops and ultra-fast acquisition system to reduce the measurement scale, both temporal and spatial. However, these techniques are mainly indirect measurements and validated numerical approach remains an extremely interesting alternative to gain information on very small spatio-temporary scales inaccessible by current experimental techniques.

From a practical point of view, liquids in industrial problems and applications involving drop coalescence, such as emulsion stability, enhanced oil recovery and ink printing as well as paint or polymeric coating, are usually non-Newtonian in nature. The drop coalescence and spreading on a surface determine often the quality of final manufactured products. The rheological properties, especially viscoelastic aspect, begin to be considered in experimental works[15]. The numerical simulation, in particular by means of the lattice Boltzmann (LB) method, remains still scarce for such complex media.

Some numerical experiments have been carried out over the past years on splashing, in particular some of them realized with axisymmetric geometry[16–19]. The coupling with a viscosity model is a new challenging area. Early LB approaches to viscoelastic fluids were based on Maxwell or Jeffreys models[20–22] and most of the recent works make use of a 2D Oldroyd-B model[23–25]. Some axisymmetric numerical experiments with the Oldroyd-B model[26,27] have been made but outside the framework of a LB approach. Recently, some LB works begin to consider the initial stage of coalescence[28–31].

This work presents a multiphase axisymmetrical lattice Boltzmann approach with high liquid/gas density ratio to investigate numerically the fast coalescence of a drop with a liquid pool of same nature. We also added an Oldroyd-B model for the viscoelasticity in relation with our experimental works involving viscoelastic non-Newtonian fluids[15], in particular polyethylene oxide (PEO) and polyacrylamide (PAAm) solutions in water.

Numerical simulations are compared with the experimental results regarding both the flow fields and the evolution of the width W of the liquid bridge between

[a)] Electronic mail: xavier.frank@inrae.fr
[b)] Electronic mail: Huai-Zhi.Li@univ-lorraine.fr

the drop and liquid surface that is created during the coalescence. A typical example of the visualization by a high-speed camera is illustrated in Figs. 1(a) (multimedia available online) and 1(b) (multimedia available online) with non-Newtonian and Newtonian fluids respectively.

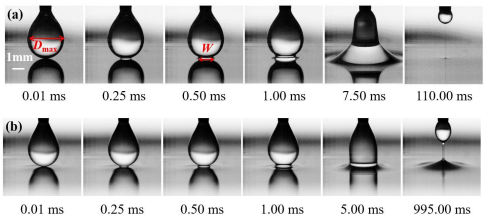

FIG. 1. Our previous experimental results of the initial coalescence[15]: (a) Viscoelastic non-Newtonian 0.5wt% Polyacrylamide (PAAm) solution with 10wt% NaCl, with an initial velocity of $v_0 = 0.29\text{mm.s}^{-1}$ (multimedia available online), (b) Water 5wt% NaCl with the same initial velocity (multimedia available online).

The paper is organized as follows. Firstly, we are presenting the theoretical aspect of the model used. Then, are detailed the numerical scheme and the associated boundary conditions with special care to the axisymmetry. Finally, the numerical results of the liquid bridge evolution are compared with the experimental visualization by a high-speed camera. Furthermore, the velocity fields issued from the numerical simulations are validated by the experimental measurements thanks to a micro-Particle Image Velocimetry (μ-PIV) device.

II. GOVERNING EQUATIONS

A. Macroscopic Equations

To avoid to define boundary conditions at the interfaces between phases, we will rely here on a diffuse interface model within the framework of the Navier-Stokes (NS) equation,

$$\rho\frac{\partial \mathbf{u}}{\partial t} + \rho\mathbf{u}\cdot\nabla\mathbf{u} = -\nabla p + \rho\nu\left(\nabla\cdot\nabla\right)\mathbf{u} + \mathbf{F} \quad (1)$$

$$\mathbf{F} = \mathbf{F}_\text{s} + \mathbf{F}_\text{oldroyd} \quad (2)$$

where $\mathbf{u}$ is the velocity field, p the pressure field, ρ the density field, $\mathbf{F}_\text{s}$ and $\mathbf{F}_\text{oldroyd}$ are forces related to interfacial tension and to viscoelasticity respectively. As the fluid is assumed incompressible in effective flow conditions, the mass conservation law leads naturally to

$$\nabla\cdot\mathbf{u} = 0 \quad (3)$$

The distribution of the phases is described using a scalar field ϕ, which obeys the Cahn-Hillard equation

$$\frac{\partial \phi}{\partial t} + \mathbf{u}\cdot\nabla\phi = \nabla\cdot(M\cdot\nabla\mu) \quad (4)$$

where $M > 0$ is the mobility and μ the chemical potential. To recover the density field ρ and the kinematic viscosity ν we use the linear relationships

$$\rho = \rho_l\phi + \rho_g(1-\phi) \quad (5)$$

$$\nu = \nu_l\phi + \nu_g(1-\phi), \quad (6)$$

where the indices l and g denote the liquid and gas phases respectively. The value of ϕ is 0 for the gas phase and 1 for the liquid phase. The interface is located at $\phi = 0.5$.

The Oldroyd-B model[32,33] is employed here to describe the viscoelasticity of non-Newtonian fluids encountered in our experiments with PEO and PAAm solutions. The velocity field $\mathbf{u}$ and the conformation tensor $\mathbf{A}$ are involved in a non linear coupling such as

$$\frac{\partial \mathbf{A}}{\partial t} + (\mathbf{u}\cdot\nabla)\mathbf{A} = -\frac{1}{\lambda}(\mathbf{A}-\mathbf{I}) + \mathbf{A}\cdot\nabla\mathbf{u} + (\nabla\mathbf{u})^T\cdot\mathbf{A} \quad (7)$$

where $\mathbf{I}$ is the unity tensor.

The viscoelastic force is computed from $\mathbf{A}$ with the following expression

$$\mathbf{F}_\text{oldroyd} = \nabla\cdot\left(\frac{\eta_p}{\lambda}(\mathbf{A}-\mathbf{I})\right) \quad (8)$$

where the viscosity η_p and the relaxation time λ are the material parameters describing polymer solutions.

B. Numerical approach

1. Lattice Boltzmann Method

The numerical scheme proposed here is similar to the model developed by Sun et al.[18] based on the approach of He et al.[34] as well as Lee and Lin.[35] to manage high fluid density ratio up to 1000. The addition of external forces comes from the work of Lee and Fischer et al.[36]. The modification into an axisymmetric geometry was made for a monophase system by Halliday et al .[37]. Then Premnath et al.[38] were the first to choose an axisymmetric model for multiphase flows. Recently Huang et al.[39] proposed a mass-conserving model by adding an equation to keep the same density ratio over the time. Some improvements have been made recently by Fakarhi et al.[40] and Chen et al.[41] through the implementation of the Cahn-Hillard equation with a new equilibrium distribution function.

At the initial time, the targeted system is axisymmetric. Given the viscosity of the fluids and the size of the drops, this symmetry is preserved until the end of the coalescence. Consequently, the flow can be correctly described by a 2D model, with the appropriate corrective terms.

For the multiphase Lattice Boltzmann model, we use a D2Q9 lattice with $\mathbf{e}_0 = (0,0)$, $\mathbf{e}_1 = (1,0)$, $\mathbf{e}_2 = (0,1)$, $\mathbf{e}_3 = (-1,0)$, $\mathbf{e}_4 = (0,-1)$,$\mathbf{e}_5 = (1,1)$, $\mathbf{e}_6 = (-1,1)$, $\mathbf{e}_7 = (-1,-1)$, $\mathbf{e}_8 = (1,-1)$, shown in Fig. 2 and the weight associated $\omega_0 = 4/9$, $\omega_{1,4} = 1/9$ and $\omega_{5,8} = 1/36$. The $\mathbf{e}_i$ vectors and all the quantities in the numerical model are expressed in LB units. Space and time steps are $\delta x = 1$ and $\delta t = 1$, respectively. To compare numerical results with experimental ones, we will rely exclusively on the relevant dimensionless numbers that characterize the flow.

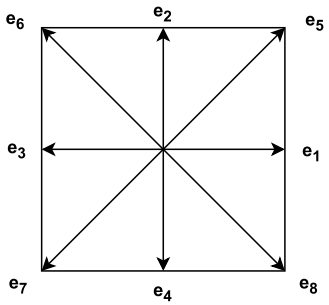

FIG. 2. D2Q9 lattice.

For the convenience, the relative axisymmetric coordinates (r, z) are written as (y, x). The model relies on a pre-stream-collide/collide/stream steps scheme. Concretely, equilibrium distribution functions are modified with initial equilibrium functions defined as follows

$$g_i^{\mathrm{eq}}(\mathbf{x},t) = \omega_i \left[p + c_s^2 \rho \left(\frac{e_{i\alpha}u_\alpha}{c_s^2} + \frac{e_{i\alpha}e_{i\beta}u_\alpha u_\beta}{2c_s^4} - \frac{u_\alpha u_\alpha}{2c_s^2} \right) \right] \tag{9a}$$

$$f_i^{\mathrm{eq}}(\mathbf{x},t) = \omega_i \phi \left[1 + \frac{e_{i\alpha}u_\alpha}{c_s^2} + \frac{e_{i\alpha}e_{i\beta}u_\alpha u_\beta}{2c_s^4} - \frac{u_\alpha u_\alpha}{2c_s^2} \right] \tag{9b}$$

and the new equilibrium functions are

$$\overline{g}_i^{\mathrm{eq}}(\mathbf{x},t) = g_i^{\mathrm{eq}}(\mathbf{x},t) - \frac{\delta t}{2}(e_{i\alpha} - u_\alpha) \Big[\partial_\alpha^{CD} \rho c_s^2 \big(\Gamma_i(\mathbf{u}) - \Gamma(0)\big) - \big(\phi \partial_\alpha^{CD} \mu - F_\alpha\big)\Gamma_i(u) - c_s^2 \omega_i \frac{u_y}{y} \Big] \tag{10a}$$

$$\overline{f}_i^{\mathrm{eq}}(\mathbf{x},t) = f_i^{\mathrm{eq}}(\mathbf{x},t) - \frac{\delta t}{2}(e_{i\alpha} - u_\alpha) \Big[\partial_\alpha^{CD} \phi - \frac{\phi}{\rho c_s^2} \Big(\partial_\alpha^{CD} p + \phi \partial_\alpha^{CD} \mu \Big) \Gamma_i(\mathbf{u}) - \omega_i \frac{\phi u_y}{y} \Big]. \tag{10b}$$

where

$$\Gamma_i(u) = \omega_i \left[1 + \frac{e_{i\alpha}u_\alpha}{c_s^2} + \frac{e_{i\alpha}e_{i\beta}u_\alpha u_\beta}{2c_s^4} - \frac{u_\alpha u_\alpha}{2c_s^2} \right] \tag{11}$$

The time evolution of $\overline{f}_i(\mathbf{x},t)$ and $\overline{g}_i(\mathbf{x},t)$ is governed by

$$\overline{g}_i(\mathbf{x} + \mathbf{e}_i\delta t, t + \delta t) = \overline{g}_i(\mathbf{x},t) - \frac{1}{\tau_g + 0.5} (\overline{g}_i(\mathbf{x},t) - \overline{g}_i^{eq}(\mathbf{x},t)) + \delta t (e_{i\alpha} - u_\alpha) \Big[\partial_\alpha^{MD} \rho c_s^2 \big(\Gamma_i(\mathbf{u}) - \Gamma(0)\big) - \big(\phi \partial_\alpha^{MD} \mu - F_\alpha\big)\Gamma_i(u) - c_s^2 \omega_i \frac{u_y}{y} \Big] \tag{12a}$$

$$\overline{f}_i(\mathbf{x} + \mathbf{e}_i\delta t, t + \delta t) = f_i(\mathbf{x},t) - \frac{1}{\tau_f + 0.5} (\overline{f}_i(\mathbf{x},t) - \overline{f}_i^{eq}(\mathbf{x},t)) + \delta t (e_{i\alpha} - u_\alpha) \Big[\partial_\alpha^{MD} \phi - \frac{\phi}{\rho c_s^2} \Big(\partial_\alpha^{MD} p + \phi \partial_\alpha^{MD} \mu \Big) \Gamma_i(\mathbf{u}) - \omega_i \frac{\phi u_y}{y} \Big] + \frac{M}{2} \Delta\mu \Gamma_i(u) \tag{12b}$$

where F_α is the α component of the total force $\mathbf{F} = \mathbf{F}_s + \mathbf{F}_{\mathrm{oldroyd}}$.

The exponents *CD* and *MD* represent the two different kinds of derivative used in this model: the central derivative and the mixed derivative respectively[36]. For the discretization of the central derivative we have

$$\delta t \cdot \mathbf{e}_i \nabla^{CD} \psi|_x = \frac{1}{2} \left[\psi(\mathbf{x} + \mathbf{e}_i \delta t) - \psi(\mathbf{x} - \mathbf{e}_i \delta t) \right] \tag{13}$$

$$\nabla^{CD} \psi|_x = \frac{1}{c_s^2 \delta t} \sum_{i \neq 0} \omega_i \mathbf{e}_i (\delta t \mathbf{e}_i \cdot \nabla^{CD}) \psi|_x \tag{14}$$

and the mixed derivative takes the form

$$\delta t \cdot \mathbf{e}_i \nabla^{MD} \psi|_x = \frac{1}{4} [-\psi(\mathbf{x} + 2\mathbf{e}_i \delta t) + 5\psi(\mathbf{x} + \mathbf{e}_i \delta t) + 3\psi(\mathbf{x}) - \psi(\mathbf{x} - \mathbf{e}_i \delta t)] \tag{15}$$

$$\nabla^{MD} \psi|_x = \frac{1}{c_s^2 \delta t} \sum_{i \neq 0} \omega_i \mathbf{e}_i (\delta t \mathbf{e}_i \cdot \nabla^{MD}) \psi|_x \tag{16}$$

where ψ is an arbitrary scalar field.

The next gradients are determined using the central derivative by default except in Eq. (12)

The Laplacian term in Cartesian coordinates is determined using the following approximation[16,36]

$$\delta^2 \psi|_{\mathbf{x}} = \frac{2}{c_s^2 \delta x} \sum_i \omega_i \Big(\psi(\mathbf{x} + \mathbf{e}_\alpha \Delta t) - \psi(\mathbf{x}) \Big) \tag{17}$$

To compute the Laplacian in cylindrical coordinates we need to add the term: $\frac{1}{y}\frac{\delta_y\psi}{y}$ so we have

$$\nabla^2\psi|_{\mathbf{x}} = \delta^2\psi|_{\mathbf{x}} + \frac{1}{y}\delta_y\psi \tag{18}$$

The surface tension $\mathbf{F}_s$ is calculated through the chemical potential μ

$$\mathbf{F}_s = -\phi\cdot\nabla\mu \tag{19}$$

where

$$\mu = 4\beta\phi(\phi-1)(\phi-0.5) - \kappa\nabla^2\phi \tag{20}$$

The parameters in Eq. 20 can be related to the surface tension σ and the interface thickness ι as $\beta = \frac{12\sigma}{\iota}$ and $\kappa = \frac{3}{2}\sigma\iota$.

The macroscopic fields are computed as follows

$$\phi = \sum_i \overline{f}_i - \phi\frac{u_y}{2y} \tag{21}$$

$$\rho c_s^2\mathbf{u} = \sum_i \overline{g}_i\mathbf{e}_i + \frac{\Delta t}{2}c_s^2\mathbf{F} \tag{22}$$

$$p = \sum_i \overline{g}_i + \frac{\Delta t}{2}u_\alpha\partial_\alpha\rho c_s^2 - \frac{1}{2}c_s^2\rho\frac{u_y}{y}\Delta t \tag{23}$$

where the density field ρ is estimated by Eq. (6).

The relaxation time τ_g is related to the fluid viscosity $\nu = c_s^2(\tau_g - 1/2)$, where $c_s = c\sqrt{1/3}$ is the lattice speed of sound, with $c = \delta x/\delta t$ and where δx and δt are the space and time step of the lattice, respectively. Finally, we choose $\tau_f = \tau_g$.

2. Oldroyd-B model

To describe the viscoelastic behaviour, we made previously use of a Maxwell model of 6$^{\text{th}}$ order for the LB simulation of a rising bubble in non-Newtonian fluids[22]. In the present work, we chose the Oldroyd-B model to compute the temporal evolution of the conformation tensor $\mathbf{A}$. To do so, we rely on a modified advection-diffusion LB scheme based on the D2Q5 lattice[23], where $\boldsymbol{\xi}_0 = (0,0)$, $\boldsymbol{\xi}_1 = (1,0)$, $\boldsymbol{\xi}_2 = (0,1)$, $\boldsymbol{\xi}_3 = (-1,0)$, $\boldsymbol{\xi}_4 = (0,-1)$, as shown in Fig. 3. The weight of the directions are $\omega_0 = 0$ and $\omega_{1,4} = 1/4$.

We define the distribution functions $h_{i\alpha\beta}$ which obey the following equations involving each component $A_{\alpha\beta}$ of the conformation tensor $\mathbf{A}$

$$\begin{aligned} h_{i\alpha\beta}(\mathbf{x}+\boldsymbol{\xi}_i\delta t, t+\delta t) &= h_{i\alpha\beta}(\mathbf{x},t) \\ &-\frac{1}{\tau_h}\Big(h_{i\alpha\beta}(\mathbf{x},t) - h^{\text{eq}}_{i\alpha\beta}(A_{\alpha\beta},\mathbf{u})\Big) \\ &+\Big(1-\frac{1}{2\tau_h}\Big)\frac{G_{\alpha\beta}}{A_{\alpha\beta}}h^{eq}_{i\alpha\beta}(A_{\alpha\beta},\mathbf{u}) \end{aligned} \tag{24}$$

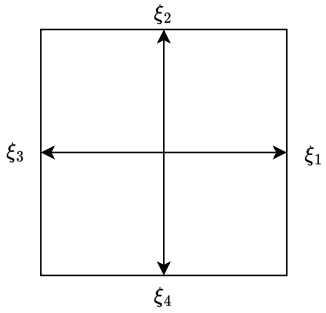

FIG. 3. D2Q5 lattice.

where the source term $\mathbf{G}$ is

$$\mathbf{G} = -\frac{1}{\lambda}(\mathbf{A}-\mathbf{I}) + \mathbf{A}\cdot(\nabla^{CD}\mathbf{u}) + (\nabla^{CD}\mathbf{u})^T\cdot\mathbf{A} \tag{25}$$

and the equilibrium functions are

$$h^{eq}_{i\alpha\beta} = \omega_i A_{\alpha\beta}\left(1 + \frac{\boldsymbol{\xi}_i\cdot\mathbf{u}}{c_l^2}\right) \tag{26}$$

The components of the conformation tensor are then computed as follows

$$A_{\alpha\beta} = \sum_i h_{i\alpha\beta} + \frac{G_{\alpha\beta}}{2} \tag{27}$$

The relaxation time τ_h is related to a diffusivity $\zeta = c_s^2(\tau_h - 1/2)$. This approach introduces diffusive terms into the equation of state. These terms stabilize the simulations but introduce errors. Following Malaspinas *et al.*[23], we fixed a diffusivity/viscosity ratio $\zeta/\eta_p \sim 10^{-6}$ to reach a suitable compromise between stability and numerical error.

This LB approach to the Oldroyd-B model has been validated for three benchmark problems[23]: 3D Taylor–Green vortex, compared with a high accuracy pseudo spectral Fourier approach; 2D simplified mill of four rolls, compared with analytical approximations; and 2D steady Poiseuille flow, compared with a classical analytical solution.

III. NUMERICAL SIMULATION AND EXPERIMENTAL APPROACH

The simulation system is discretized on a regular grid of resolution 800×400. To avoid the singularity related to the factor $\frac{u_y}{y}$, the grid starts at the position $\delta x/2$ in

the y direction[42]. Due to the symmetry, mirror boundary conditions are imposed on the axis, i.e. $\overline{g}_2 = \overline{g}_4$, $\overline{g}_6 = \overline{g}_7$, $\overline{g}_5 = \overline{g}_8$ and $\overline{f}_2 = \overline{f}_4$, $\overline{f}_6 = \overline{f}_7$, $\overline{f}_5 = \overline{f}_8$. Half-bounce back boundary conditions are imposed everywhere else. These boundaries are applied after the streaming step (see Sun et al.[18] for more details).

Fig. 4 is a schematic representation of the initial state of the simulated system, a drop just above a planar surface of the same liquid. The liquid pool is a layer of depth L and the drop is a disk of a diameter $D_{\max}$ and center $\mathbf{x}^D = (L + L_G + D_{\max}/2, 0)$, where L_G is the size of an initial gap between the liquid surface and the bottom of the drop.

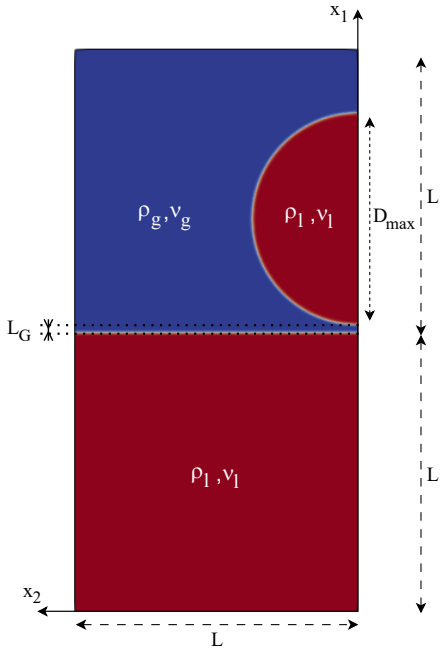

FIG. 4. Schematic representation of the initial state at the beginning of the simulation. Color indicates the index field ϕ. The liquid ($\phi = 1$) appears in red and the gas ($\phi = 0$) appears in blue.

The initial drop diameter is $D_{\max} = 300$, the pool depth is $L = 400$ and the size of the gap is $L_G = 15$. The main difference between the simulations and the experiments is due to the method used to trigger the coalescence. In the experiments, an initial velocity is imposed to the pendant drop as the fluid is slowly injected through the nozzle by a micropump. On the contrary, in numerical simulations, the coalescence triggers spontaneously. The initial velocity in experiments is chosen to be as small as possible, and once coalescence is triggered, this difference has no impact on subsequent phenomena. The initial index field is set to be

$$\phi(\mathbf{x}) = f(x_1 - L) + f\left(\|\mathbf{x} - \mathbf{x}^D\| - \frac{D_{\max}}{2}\right)$$
$$f(a) = \frac{1}{2}\left(1 - \tanh\frac{a}{\iota}\right) \quad (28)$$

where the interface thickness is $\iota = 4$. The density ratio is $\rho_l/\rho_g = 1000$ and the viscosity ratio is $\nu_l/\nu_g = 300$.

We made use of three distinct techniques to investigate experimentally the fast coalescence at small spatio-temporary scales[15]:

- a home-made direct current (DC) electrical circuit based on an improved Howland current source at the early coalescence stage by relating the electrical conductance to the coalescing section;
- a high-speed camera Phantom V711 (Vision Research, USA) equipped with a macro lens (EF 100mm f/2.8, Canon, Japan) from the side view for the superimposed transition with the above electrical system and beyond;
- a home-developed high-speed micro-Particle Image Velocimetry (μ-PIV) technique to follow the flow field during the coalescence both in the drop and the liquid surface.

For the μ-PIV technique, a small amount of silver coated hollow glass spheres (S-HGS-10, Dantec Dynamics, Denmark) with an average diameter of 10 μm or fluorescence particles (MF-RhB-Partikel-G020, Dantec Dynamics, Denmark) with a diameter of 1-20 μm were added in aqueous Newtonian and non-Newtonian liquids. Two lasers (LaserMax Inc., USA) of 1 mW were placed in the opposite direction to excite seeding particles in the laser sheet located inside the pendant drop and liquid pool. The images were captured by the high-speed camera Phantom V711 coupled with a zoom lens (MP-E 65mm f/2.8, Canon, Japan) and velocities were computed up to 4000 flow fields/s.

Three different liquids were employed in the experiments, including distilled water, $1wt\%$ polyethylene oxide (PEO) with molecular weights of $5\times10^6 g.mol^{-1}$ in water, $0.5wt\%$ polyacrylamide (PAAm) with molecular weight of $1.3 \times 10^7 g.mol^{-1}$ in water. To strengthen the liquid electrical conductivity, $5wt\%$ or $10wt\%$ NaCl was added in the solutions. The rheological properties of PEO and PAAm solutions were characterized by a rheometer (AR-G2, TA Instruments, USA) and displayed viscoelastic and shear-thinning behavior. According to the relaxation characterization on the rheometer and within the shear rate range corresponding to the coalescence, the Deborah number De varies from 3.9 to 19.3 for the PEO solution and from 4.5 to 24.1 for the PAAm solution respectively. The concentration of these polymers in water was in the semi-diluted regime.

The air trapping occurs usually for the case of drop or solid impact on a liquid surface. In our experiments, the approaching velocity of a pendant drop towards the planar liquid pool was varied from 0.06 to 0.29 mm.s^{-1} and no difference was effectively observed for the coalescence in this range, especially for the air trapping phenomenon. In this work, the maximum approaching velocity of 0.29 mm.s^{-1} without effect on coalescence was used to compare with the LB simulation as shown in Fig. 1 and multimedia Fig. 1a & multimedia Fig. 1b. Compared to the drop or solid impact which is much more rapid so that the air film between the drop or solid and the liquid pool cannot be evacuated in time. In our experiments, this phenomenon is avoided voluntarily to not add complexity to the coalescence. The ultra-fast monitoring of DC electric signals confirms clearly this evidence as the presence of air film does n't allow the measurements of coalescing width.

In the case of Oldroyd-B fluids for the numerical simulation, the non-Newtonian viscoelasticity/Newtonian viscosity ratio is $\eta_p/\eta_l = 1000$. In this study, we compare the numerical simulations with our previous experimental results[15] in two cases: viscous Newtonian fluid and viscoelastic fluid. The relevant dimensionless numbers are the Ohnesorge number $Oh = \eta_l/\sqrt{\rho_l D_{\max}\sigma}$, which relates the viscous force to inertia and surface tension, the Bond number $Bo = \Delta\rho g W^2/\sigma$, which compares the gravity to surface tension and the Deborah number $De = \dot{\gamma}\lambda$, where $\dot{\gamma}$ is the shear rate. The numerical De varies around 20 in our simulations. During the time interval of the simulation, the highest value of Bond number $Bo_{\max}$ is reached when $W = D_{\max}$. As $Bo_{\max} = 0.56$, the gravity does not play a crucial role, especially during the first steps of the coalescence. The viscoelastic properties of fluids are varied through the relaxation parameter λ in the Odroyld-B model. We choose several values ranging from $\lambda = 1 \times 10^4$ to $\lambda = 5 \times 10^4$. This corresponds to the domain for the Deborah number De from 4.0 to 20.0, then covers the experimentally investigated range. It is worth noting the numerical results remain unchanged for the simulated Deborah number De range, as detailed in the following results.

IV. RESULTS AND DISCUSSION

In this study, the origin of time $t = 0$ is fixed at the first contact between the drop and the liquid surface, when the liquid bridge appears. As the coalescence triggers spontaneously, this starting point has to be detected. Given the symmetry of the system, the contact necessarily occurs on the axis. Let's consider a segment $[AB]$ between the bottom of the bath ($x = 0$ and $y = 0$) and a point below the top of the drop (the center of the initial drop, for example). As explained in part II A, the gas/liquid interface is located on points where $\phi = 0.5$. Straightforwardly, if $\min_{[AB]}(\phi) < 0.5$, the liquid bridge does not exist and if $\min_{[AB]}(\phi) \geq 0.5$, liquid bridge does exist. We detect the first contact and fix the origin of the time using the transition between these two situations (Fig. 5). The initial position of the contact is $\mathbf{x}^c = (x_1^c, 0)$.

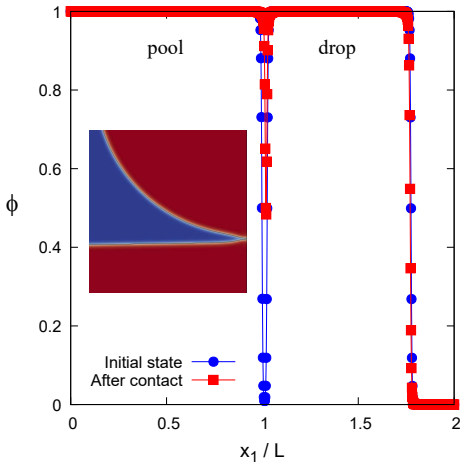

FIG. 5. Value of ϕ along the symmetry axis at two distinct times: the initialization of the simulation and just after the contact between the drop and the liquid surface ($t = 0$). The locations on the x_1/L interval of pool and drop, respectively are shown to guide the eye. Inset: snapshot of the ϕ field at the date $t = 0$. The liquid ($\phi = 1$) appears in red and the gas ($\phi = 0$) appears in blue.

In the following, we use a dimensionless time

$$\begin{aligned} t^* &= t/t_i \\ t_i &= \sqrt{\rho_l {D_{\max}}^3/\sigma} \end{aligned} \tag{29}$$

where t_i is the inertial time[15].

As soon as the drop comes into contact with the bath, a liquid bridge forms and begins to expand [Fig. 6 (multimedia available online)]. This observation is in good agreement with the experimental findings [Figs. 1(a) (multimedia available online) and 1(b) (multimedia available online)].

Figure 7 shows two successive snapshots of the velocity field in an Oldroyd-B fluid, predicted by LB simulations. In the first step of coalescence, the flow in the liquid bridge is purely radial (Fig. 7a). Fig. 8 displays a comparison between the experimental velocity field captured by μ-PIV[15] and the one from LB simulation. The initial approaching velocity for the experiments was 0.29 mm.s^{-1} with the scale of the velocity vector 0.2mm. For the numerical simulation, the scale is set to be $3,6 \times 10^{-3}$ lattice units. The recirculation in the liquid bridge predicted by the LB simulation compares favourably with

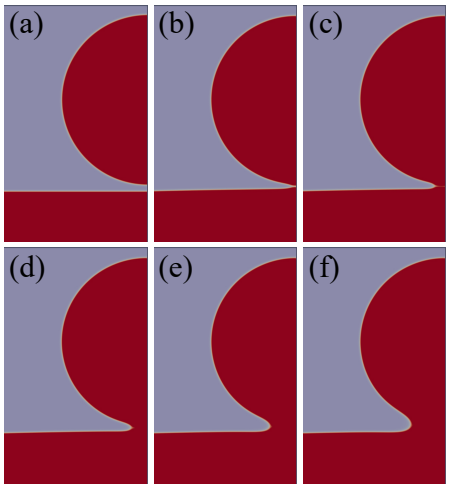

FIG. 6. Snapshots of the liquid bridge simulated by the Oldroyd-B fluid with $\lambda = 1 \times 10^4$ and $De = 4.0$ (multimedia available online). (a) $t^* = 0$, (b) $t^* = 1.35 \times 10^{-4}$, (c) $t^* = 9.75 \times 10^{-4}$, (d) $t^* = 2.40 \times 10^{-3}$, (e) $t^* = 6.13 \times 10^{-3}$, (f) $t^* = 9.70 \times 10^{-3}$

the experimental measurements obtained by the μ-PIV technique. With increasing t^* (Fig. 7b), a slight difference can be observed regarding the flow fields around the central axis between the LB simulation and the experimental measurements. The motion is ascending just around the axe for the LB simulation, while the μ-PIV results reveal a downstream in whole the drop. This can be explained by the continuous feeding of a liquid flowrate in the coalescence experiments. On the other hand, an isolated drop without feeding is simulated by the LB approach.

The width W of the bridge is computed as follows. Let's consider the collinear line with $\mathbf{e}_2$ and starting from $\mathbf{x}^c$. The position of the interface on this line is $\mathbf{x}^i = (x_1^c, W/2)$, where W is the width of the bridge. Then, we can deduce the normalized width Φ following

$$\Phi = \frac{W}{D_{\max}} \tag{30}$$

Figure 9 shows the evolution of Φ as a function of t^*. Numerical results are compared with the experimental data, obtained with water, 1wt% Polyethylene oxides (PEO) solution and 0.5wt% Polyacrylamide (PAAm) solution respectively. The rheological properties of these fluids can be found in our previous work[15]. The normalized width $\Phi(t^*)$ is satisfactorily simulated over a wide range of time t^*. For t^* ranging from 3×10^{-5} to 5×10^{-3}, a good agreement between the numerical results and experimental data can be observed. In both approaches, the normalized width $\Phi(t^*)$ obeys a power law of t^{*1} in

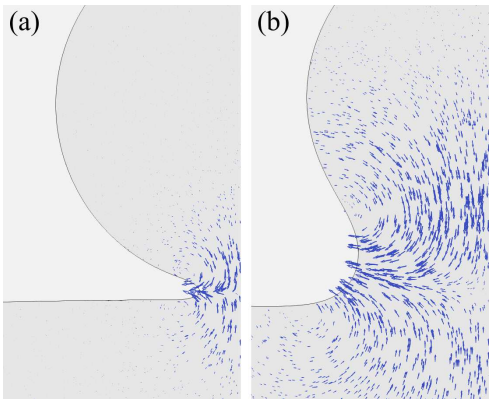

FIG. 7. Velocity field and drop interface from LB simulation. Oldroyd-B fluid with $\lambda = 1 \times 10^4$ and $De = 4.0$. (a) $t^* = 6.13 \times 10^{-3}$, (b) $t^* = 1.05 \times 10^{-1}$.

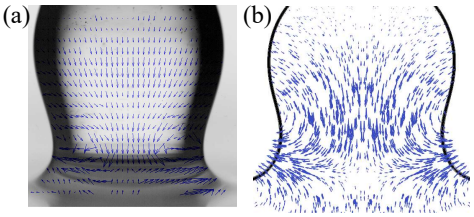

FIG. 8. Comparison of the velocity fields between the experiments by μ-PIV technique and LB numerical simulation. (a) 0.5wt% PAAm (b) Oldroyd-B fluid with $\lambda = 5 \times 10^4$ and $De = 20.0$

.

the so-called inertially limited viscous regime. The simulated bridge's size Φ in function of $t^{*1/2}$ compares well with the experimental observation for longer time t^* in the inertial regime.

In the case of the most viscoelastic fluid with $\lambda = 5 \times 10^4$ and $De = 20.0$ corresponding to the PAAm solution in our experiments, the simulated width is overestimated but still obeys a satisfactory evolution dynamics compared to the experiments. Fig. (9) also shows that the relaxation parameter λ affects slightly the evolution of the bridge size. The same effect can be spotted in the experimental results. The rheological model of Oldroyd-B used in this work is better justified compared to the Maxwell model of 6^{th} order adopted in our group in the past to simulate a rising bubble in non-Newtonian fluids. It is also worth noting that whatever the model used to describe the viscoelasticity of fluids, Maxwell or Oldroyd-B, the smallest time scale notably accessible on a rheometer of order of 100 ms is largely greater than the

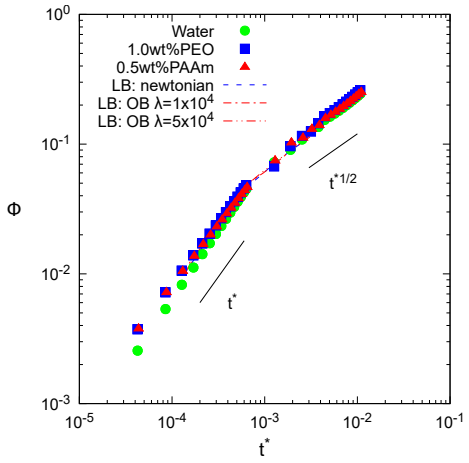

FIG. 9. Evolution of the dimensionless width Φ of the liquid bridge as a function of the normalized time t^*. Experimental data obtained with various fluids and numerical results from various rheological models. The black continuous line shows a power law with an exponent 1 and 1/2, used to guide the eye.

entire duration of the coalescence, typically less than 50 ms. This explains partly the relatively limited effect of the viscoelastic models employed here in the LB approach or other other numerical schemes in the literature.

From a physical point of view, for the PAAm solutions having the highest molecular weight among the fluids used here, the radius of gyration measured by the multi-angle light scattering (MALS, Wyatt Technology, USA) is $R_g = 101.70$ nm, then well below the smallest monitored scale by the electrical device and the high-speed camera that is superior to 7.4 μm. The numerical details described either the current LB or other approaches cannot address successfully such a spatial scale yet.

V. CONCLUSION

We carried out numerical lattice Boltzmann simulation on the initial coalescence of a drop with a pool of the same liquid. Both Newtonian and viscoelastic fluids were investigated by relying on an axisymmetric multiphase LB approach with high density ratio coupled with an Oldroyd-B model. Just after the initial contact, a liquid bridge formed between the drop and the pool. The subsequent dynamics was then governed by the fast widening of this bridge. Firstly, we observed that the predicted flow fields exhibit a recirculating pattern similar to that captured experimentally with the help of μ-PIV. Then, we studied the temporary evolution of the width of the liquid bridge, gathered in dimensionless form by the initial drop diameter and the inertial time, respectively. In both Newtonian and viscoelastic fluids, the rescaled width Φ of the bridge evolved linearly with the normalized time t^* during the first step of the coalescence in the inertially limited viscous regime, followed by a power law Φ vs. $t^{*1/2}$ in the inertial regime for longer time. A satisfactory agreement is observed between the numerical simulations and the experimental results. However, further investigation is still required to develop reliable rheological models for the numerical simulation of extremely small spatial and temporary scales.

ACKNOWLEDGMENTS

The PhD fellowship from the French Ministry of Higher Education, Research and Innovation to E. Collignon is gratefully acknowledged.

[1] J. Eggers, J. R. Lister, and H. A. Stone, "Coalescence of liquid drops," Journal of Fluid Mechanics **401**, 293–310 (1999).
[2] M. Rein, "The transitional regime between coalescing and splashing drops," Journal of Fluid Mechanics **306**, 145–165 (1996).
[3] A. I. Fedorchenko and A.-B. Wang, "On some common features of drop impact on liquid surfaces," Physics of Fluids **16**, 1349–1365 (2004).
[4] M. Geri, B. Keshavarz, G. H. McKinley, and J. W. M. Bush, "Thermal delay of drop coalescence," Journal of Fluid Mechanics **833**, R3 (2017).
[5] F. Blanchette and T. P. Bigioni, "Partial coalescence of drops at liquid interfaces," Nature Physics **2**, 254–257 (2006).
[6] M. Yokota and K. Okumura, "Dimensional crossover in the coalescence dynamics of viscous drops confined in between two plates," Proceedings of the National Academy of Sciences **108**, 6395–6398 (2011).
[7] F. Blanchette, L. Messio, and J. W. M. Bush, "The influence of surface tension gradients on drop coalescence," Physics of Fluids **21**, 072107 (2009).
[8] F. Marcotte, G.-J. Michon, T. Séon, and C. Josserand, "Ejecta, Corolla, and Splashes from Drop Impacts on Viscous Fluids," Physical Review Letters **122**, 014501 (2019).
[9] S. Shim and H. A. Stone, "Damped coalescence cascade of liquid drops," Physical Review Fluids **2**, 044001 (2017).
[10] J. D. Paulsen, J. C. Burton, S. R. Nagel, S. Appathurai, M. T. Harris, and O. A. Basaran, "The inexorable resistance of inertia determines the initial regime of drop coalescence," Proceedings of the National Academy of Sciences of the United States of America **109**, 6857–6861 (2012).
[11] J. F. Hernández-Sánchez, L. A. Lubbers, A. Eddi, and J. H. Snoeijer, "Symmetric and Asymmetric Coalescence of Drops on a Substrate," Physical Review Letters **109**, 184502 (2012).
[12] J. D. Paulsen, R. Carmigniani, A. Kannan, J. C. Burton, and S. R. Nagel, "Coalescence of bubbles and drops in an outer fluid," Nature communications **5**, 3182 (2014).
[13] H. P. Kavehpour, "Coalescence of Drops," Annual Review of Fluid Mechanics **47**, 245–268 (2015).
[14] S. C. Case and S. R. Nagel, "Coalescence in low-viscosity liquids," Physical Review Letters **100**, 084503 (2008).
[15] Q. Zhang, X. Jiang, D. Brunello, T. Fu, C. Zhu, Y. Ma, and H. Z. Li, "Initial coalescence of a drop at a planar liquid surface," Physical Review E **100**, 033112 (2019).
[16] L. Amaya-Bower and T. Lee, "Single bubble rising dynamics for moderate Reynolds number using Lattice Boltzmann Method," Computers & Fluids **39**, 1191–1207 (2010).

[17]J. G. Zhou, "Axisymmetric lattice Boltzmann method," Physical Review E **78**, 036701 (2008).
[18]K. Sun, M. Jia, and T. Wang, "Numerical investigation of head-on droplet collision with lattice Boltzmann method," International Journal of Heat and Mass Transfer **58**, 260–275 (2013).
[19]X. Xu, Y. Hu, Y. He, J. Han, and J. Zhu, "Modified radius-weighted lattice Boltzmann model to address singularities in axisymmetric multiphase flows," Physical Review E **106**, 025316 (2022).
[20]I. Ispolatov and M. Grant, "Lattice boltzmann method for viscoelastic fluids," Phys. Rev. E **65**, 056704 (2002).
[21]P. Lallemand, D. d'Humières, L.-S. Luo, and R. Rubinstein, "Theory of the lattice boltzmann method: Three-dimensional model for linear viscoelastic fluids," Phys. Rev. E **67**, 021203 (2003).
[22]X. Frank and H. Z. Li, "Negative wake behind a sphere rising in viscoelastic fluids: A lattice Boltzmann investigation," Physical Review E **74**, 056307 (2006).
[23]O. Malaspinas, N. Fiétier, and M. Deville, "Lattice Boltzmann method for the simulation of viscoelastic fluid flows," Journal of Non-Newtonian Fluid Mechanics **165**, 1637–1653 (2010).
[24]D. Wang, D. Tan, and N. Phan-Thien, "A lattice Boltzmann method for simulating viscoelastic drops," Physics of Fluids **31**, 073101 (2019).
[25]V. Dzanic, C. From, and E. Sauret, "A hybrid lattice boltzmann model for simulating viscoelastic instabilities," Computers & Fluids **235**, 105280 (2022).
[26]E. Turkoz, J. M. Lopez-Herrera, J. Eggers, C. B. Arnold, and L. Deike, "Axisymmetric simulation of viscoelastic filament thinning with the Oldroyd-B model," Journal of Fluid Mechanics **851**, R2 (2018).
[27]M. F. Tomé, L. Grossi, A. Castelo, J. A. Cuminato, S. McKee, and K. Walters, "Die-swell, splashing drop and a numerical technique for solving the Oldroyd B model for axisymmetric free surface flows," Journal of Non-Newtonian Fluid Mechanics **141**, 148–166 (2007).
[28]T. Scheel, Q. Xie, M. Sega, and J. Harting, "Viscous to inertial coalescence of liquid lenses: A lattice Boltzmann investigation," Physical Review Fluids **8**, 074201 (2023).
[29]P. J. Dekker, M. A. Hack, W. Tewes, C. Datt, A. Bouillant, and J. H. Snoeijer, "When Elasticity Affects Drop Coalescence," Physical Review Letters **128**, 028004 (2022).
[30]P. R. Kaneelil, A. A. Pahlavan, N. Xue, and H. A. Stone, "Three-Dimensional Self-Similarity of Coalescing Viscous Drops in the Thin-Film Regime," Physical Review Letters **129**, 144501 (2022).
[31]M. Heinen, M. Hoffmann, F. Diewald, S. Seckler, K. Langenbach, and J. Vrabec, "Droplet coalescence by molecular dynamics and phase-field modeling," Physics of Fluids **34**, 042006 (2022).
[32]J. G. Oldroyd and A. H. Wilson, "On the formulation of rheological equations of state," Proceedings of the Royal Society of London. Series A. Mathematical and Physical Sciences **200**, 523–541 (1950).
[33]V. V. Pukhnachev, "Mathematical model of an incompressible viscoelastic maxwell medium," Journal of applied mechanics and technical physics **51**, 546–554 (2010).
[34]X. He, S. Chen, and R. Zhang, "A Lattice Boltzmann Scheme for Incompressible Multiphase Flow and Its Application in Simulation of Rayleigh–Taylor Instability," Journal of Computational Physics **152**, 642–663 (1999).
[35]T. Lee and C.-L. Lin, "A stable discretization of the lattice Boltzmann equation for simulation of incompressible two-phase flows at high density ratio," Journal of Computational Physics **206**, 16–47 (2005).
[36]T. Lee and P. F. Fischer, "Eliminating parasitic currents in the lattice Boltzmann equation method for nonideal gases," Physical Review E **74**, 046709 (2006).
[37]I. Halliday, L. A. Hammond, C. M. Care, K. Good, and A. Stevens, "Lattice Boltzmann equation hydrodynamics," Physical Review E **64**, 011208 (2001).
[38]K. N. Premnath and J. Abraham, "Lattice Boltzmann model for axisymmetric multiphase flows," Physical Review E **71**, 056706 (2005).
[39]H. Huang, J.-J. Huang, and X.-Y. Lu, "A mass-conserving axisymmetric multiphase lattice Boltzmann method and its application in simulation of bubble rising," Journal of Computational Physics **269**, 386–402 (2014).
[40]A. Fakhari, M. Geier, and T. Lee, "A mass-conserving lattice Boltzmann method with dynamic grid refinement for immiscible two-phase flows," Journal of Computational Physics **315**, 434–457 (2016).
[41]G.-Q. Chen, H. Li, P. Lv, and H. Duan, "An improved multiphase lattice Boltzmann flux solver with phase interface compression for incompressible multiphase flows," Physics of Fluids **35**, 013310 (2023).
[42]H. Liang, Z. H. Chai, B. C. Shi, Z. L. Guo, and T. Zhang, "Phase-field-based lattice Boltzmann model for axisymmetric multiphase flows," Physical Review E **90**, 063311 (2014).